

Scaling of global properties of fluctuating streamwise velocities in pipe flow: Impact of the viscous term

Nils T. Basse^a

^a*Independent Scientist
Trubadurens väg 8, 423 41 Torslanda, Sweden*

September 27, 2021

Abstract

We extend the procedure outlined in [Basse, "Scaling of global properties of fluctuating and mean streamwise velocities in pipe flow: Characterization of a high Reynolds number transition region," Phys. Fluids **33**, 065127 (2021)] to study global, i.e. radially averaged, scaling of streamwise velocity fluctuations. A viscous term is added to the log-law scaling which leads to the existence of a mathematical abstraction which we call the "global peak". The position and amplitude of this global peak are characterized and compared to the inner and outer peaks. A transition at a friction Reynolds number of order 10000 is identified. Consequences for the global peak scaling, non-zero asymptotic viscosity, turbulent energy production/dissipation and turbulence intensity scaling are appraised along with the impact of including an additional wake term.

1. Introduction

Global, i.e. radially averaged, log- and power-law models for the mean and fluctuating parts of streamwise velocities in pipe flow have been presented in [1] based on Princeton Superpipe measurements [2]. In our paper, we treated log- and power-law models with two fit parameters and explained how this could be extended to e.g. three fit parameters. Here, we provide a first example of this using the log-law for streamwise velocity fluctuations, but with an additional viscous term as introduced in [3, 4].

The standard expression for streamwise velocity fluctuations is the two-parameter log-law which is a consequence of the attached eddy hypothesis

Email address: `nils.basse@npb.dk` (Nils T. Basse)

[5, 6, 7].

The square of the normalised fluctuating velocity is $\overline{u^2}/U_\tau^2$, where u is the fluctuating velocity (overbar is time averaging) and U_τ is the friction velocity. In the literature, the square of the normalised fluctuating velocity is sometimes called the turbulence intensity (TI). However, we define the TI as $I^2 = \overline{u^2}/U^2$, where U is the mean velocity. One important motivation for the study is that we saw indications of a possible Reynolds number dependence of the normalised fluctuating velocity, see e.g. Figure 4 in [1].

The paper is organized as follows: In Section 2 we review local scaling of streamwise velocity fluctuations with an additional viscous term. The radial averaging definitions which are applied to fluctuating velocities are presented in Section 3. The global scaling results are contained in Section 4. We discuss our findings in Section 5 and conclude in Section 6.

2. Local scaling

We use an equation for the normalised fluctuating velocity including the viscous term V as formulated in [4]:

$$\frac{\overline{u_l^2}(z)}{U_\tau^2} = B_l - A_l \log(z/\delta) - C_l(z^+)^{-1/2} \quad (1)$$

$$= B_l - A_l \log(z/\delta) + V(z^+), \quad (2)$$

where z is the distance from the wall, δ is the boundary layer thickness (pipe radius R for pipe flow) and $z^+ = zU_\tau/\nu$ is the normalized distance from the wall z , where ν is the kinematic viscosity. Note that:

$$z/\delta = \frac{z^+}{Re_\tau}, \quad (3)$$

where $Re_\tau = \delta U_\tau/\nu$ is the friction Reynolds number.

In [4], the fit parameters $A_l = 0.90$, $B_l = 2.67$, $C_l = 6.06$, see Figure 1 for an example. Here, A_l and C_l are universal constants and B_l is a "large-scale characteristic constant", i.e. dependent on the specific geometry. The subscript "l" means that the constants are "local" fits, i.e. a range of z where the model is valid ($z^+ > 50$ [8]).

Similar [9] and more complex [10] viscous terms $V(z^+)$ have been treated previously. We use a simple term for clarity of exposition and to show the qualitative behaviour.

The viscous term has an exponent of $-1/2$, which is close to what we found when fitting a two-parameter power-law to the radially averaged measurements [1]:

$$\left. \frac{\overline{u_g^2(z)}}{U_\tau^2} \right|_{\text{power-law}} = [1.24 \pm 0.04] \times \left(\frac{z}{\delta} \right)^{-0.48 \pm 0.01}, \quad (4)$$

where the subscript "g" means that the parameters are "global", i.e. covering the entire range of z . We will return to this exponent when we discuss results of including both the viscous and wake [10, 11, 12] terms in Appendix B.

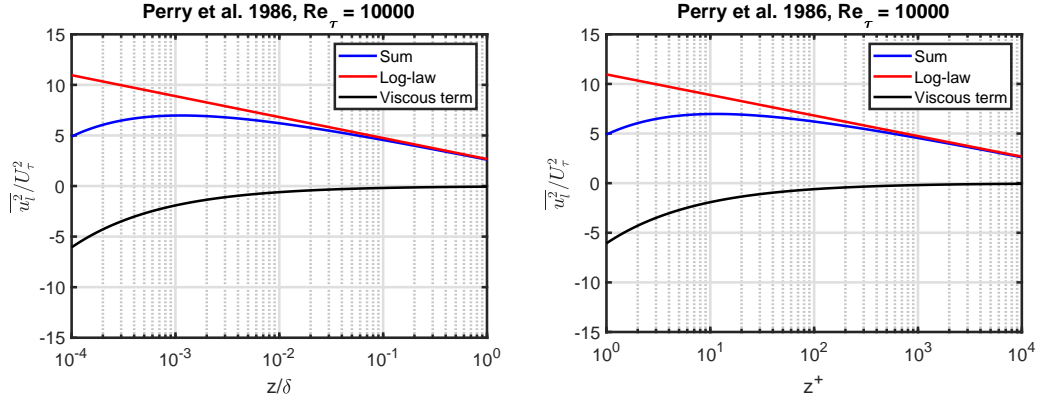


Figure 1: $\frac{\overline{u_l^2(z)}}{U_\tau^2}$ for $Re_\tau = 10000$ using fit parameters from [4] as a function of z/δ (left-hand plot) and z^+ (right-hand plot).

Adding a viscous term means that what we term a "global peak" will exist at a normalized distance from the wall given by:

$$z^+|_{\text{global peak}} = \left(\frac{C_l}{2A_l} \right)^2 \quad (5)$$

$$= 11 \quad (6)$$

This value is closer to the wall than the expected validity of the model ($z^+ > 50$), so we interpret this peak as a mathematical abstraction in some sense. However, it is interesting to note that the position is quite close to what has been measured for the so-called "inner peak" [13]:

$$z^+|_{\text{inner peak}} = 15 \quad (7)$$

Combining Equations (1) and (5) we find that the amplitude of the square of the normalised fluctuating velocity scales as:

$$\begin{aligned} \left. \frac{\overline{u_l^2}}{U_\tau^2} \right|_{\text{global peak}} &= B_l - 2A_l \times (1 + \log(C_l) - \log(2A_l)) + A_l \log(Re_\tau) \quad (8) \\ &= 0.90 \times \log(Re_\tau) - 1.32, \quad (9) \end{aligned}$$

see Figure 2.

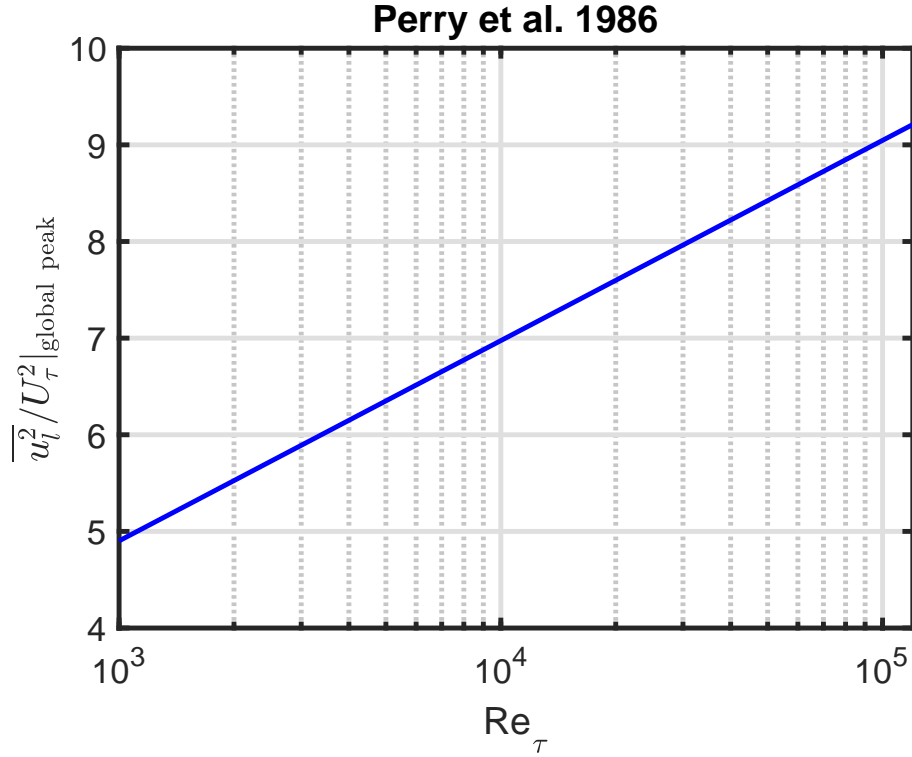


Figure 2: $\left. \frac{\overline{u_l^2}}{U_\tau^2} \right|_{\text{global peak}}$ as a function of Re_τ using fit parameters from [4].

3. Radial averaging definitions

Radial averaging is defined in Equations (10)-(15) for arithmetic mean (AM), area-averaged (AA) and volume-averaged (VA), respectively. The definitions are written both using z and z^+ .

$$\langle \cdot \rangle_{\text{AM}} = \frac{1}{\delta} \int_0^\delta [\cdot] dz \quad (10)$$

$$= \frac{1}{Re_\tau} \int_0^{Re_\tau} [\cdot] dz^+ \quad (11)$$

$$\langle \cdot \rangle_{\text{AA}} = \frac{2}{\delta^2} \int_0^\delta [\cdot] \times (\delta - z) dz \quad (12)$$

$$= \frac{2}{Re_\tau} \int_0^{Re_\tau} [\cdot] dz^+ - \frac{2}{Re_\tau^2} \int_0^{Re_\tau} [\cdot] \times z^+ dz^+ \quad (13)$$

$$\langle \cdot \rangle_{\text{VA}} = \frac{3}{\delta^3} \int_0^\delta [\cdot] \times (\delta - z)^2 dz \quad (14)$$

$$= \frac{3}{Re_\tau} \int_0^{Re_\tau} [\cdot] dz^+ + \frac{3}{Re_\tau^3} \int_0^{Re_\tau} [\cdot] \times (z^+)^2 dz^+ - \frac{6}{Re_\tau^2} \int_0^{Re_\tau} [\cdot] \times z^+ dz^+ \quad (15)$$

4. Global scaling results

4.1. Measurements

The Princeton Superpipe measurements we analyze have a maximum $Re_\tau = 98190$, whereas direct numerical simulations (DNS) currently have maximum values around 6000 [14, 15]. Thus, we continue to rely solely on measurements for $Re_\tau > 6000$. This is important for our investigation since it will become clear that a transition takes place for $Re_\tau > 10000$. Globally averaged measurements of the streamwise square of the normalised fluctuating velocity are presented in Figure 3. The measurements constitute the foundation of the results presented in the remainder of this paper.

All fits shown in our paper are fits to smooth pipe measurements, the rough pipe measurements are shown for reference.

4.2. Model

Analytical integration of Equation (1) using Equations (10)-(15) yields these three equations with the three unknowns A_g , B_g and C_g :

$$\left\langle \frac{\overline{u_g^2}}{U_\tau^2} \right\rangle_{\text{AM}} = B_g + A_g - \frac{2C_g}{\sqrt{Re_\tau}} \quad (16)$$

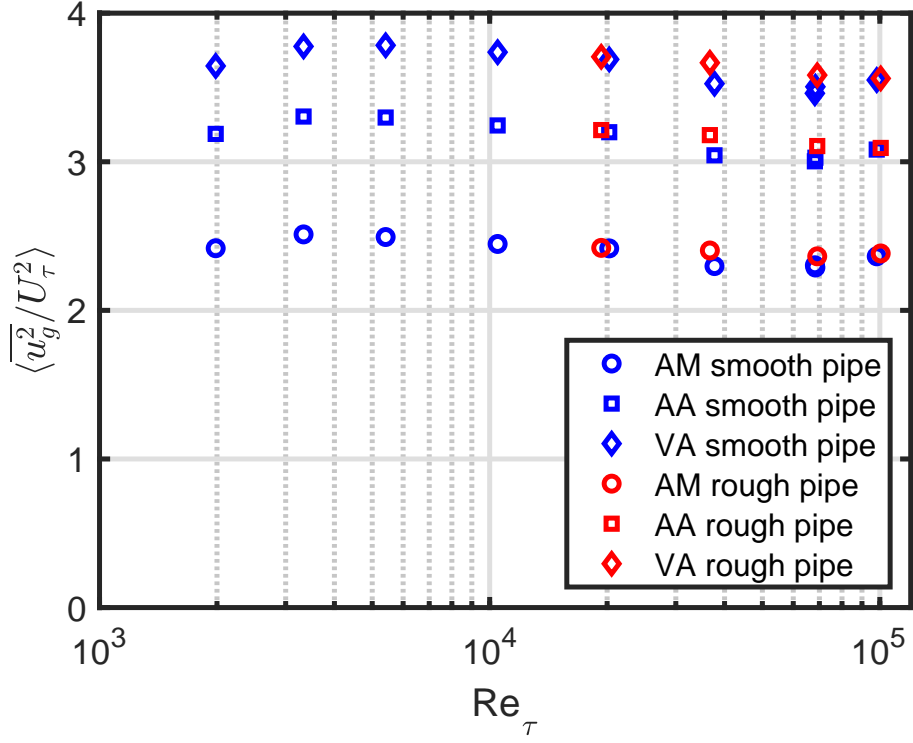


Figure 3: The averaged square of the measured normalized fluctuating velocities as a function of Reynolds number.

$$\left\langle \frac{\overline{u_g^2}}{U_\tau^2} \right\rangle_{AA} = B_g + \frac{3}{2} \times A_g - \frac{8C_g}{3\sqrt{Re_\tau}} \quad (17)$$

$$\left\langle \frac{\overline{u_g^2}}{U_\tau^2} \right\rangle_{VA} = B_g + \frac{11}{6} \times A_g - \frac{16C_g}{5\sqrt{Re_\tau}} \quad (18)$$

The solutions to these three equations are:

$$A_g = -12 \times \left\langle \frac{\overline{u_g^2}}{U_\tau^2} \right\rangle_{AM} + 27 \times \left\langle \frac{\overline{u_g^2}}{U_\tau^2} \right\rangle_{AA} - 15 \times \left\langle \frac{\overline{u_g^2}}{U_\tau^2} \right\rangle_{VA} \quad (19)$$

$$B_g = -2 \times \left\langle \frac{\overline{u_g^2}}{U_\tau^2} \right\rangle_{AM} + \frac{21}{2} \times \left\langle \frac{\overline{u_g^2}}{U_\tau^2} \right\rangle_{AA} - \frac{15}{2} \times \left\langle \frac{\overline{u_g^2}}{U_\tau^2} \right\rangle_{VA} \quad (20)$$

$$C_g = \sqrt{Re_\tau} \quad (21)$$

$$\times \left(-\frac{15}{2} \times \left\langle \frac{\overline{u_g^2}}{U_\tau^2} \right\rangle_{\text{AM}} + \frac{75}{4} \times \left\langle \frac{\overline{u_g^2}}{U_\tau^2} \right\rangle_{\text{AA}} - \frac{45}{4} \times \left\langle \frac{\overline{u_g^2}}{U_\tau^2} \right\rangle_{\text{VA}} \right) \quad (22)$$

We show examples of the resulting global profiles of the streamwise square of the normalised fluctuating velocity in Figures 4 and 5 for the lowest ($Re_\tau = 1985$) and highest ($Re_\tau = 98190$) Reynolds numbers measured. The change of the log-law part with Reynolds number is modest, but the difference for the viscous term is significant; we will quantify this below. Note that a peak is visible for the low Reynolds number measurements but not visible for the high Reynolds number, probably because the measurements are not available close to the wall. The sum of the log-law and viscous terms is seen to be negative towards the wall for the low Reynolds number case which is the solution to the system of equations in a global sense but not physical in a local sense - locally, our study is a mathematical abstraction.

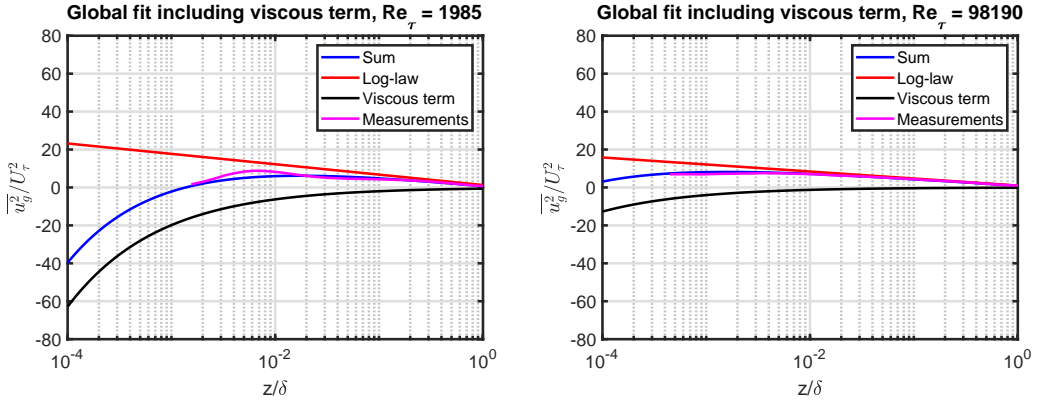


Figure 4: $\frac{\overline{u_g^2}(z)}{U_\tau^2}$ using Equation (1) and the global fit parameters as a function of z/δ . Left-hand plot: Lowest measured Re_τ , right-hand plot: Highest measured Re_τ .

4.3. Parameter fits

We now turn to the topic of whether the global fit parameters scale with Re_τ . It is clear from Figures 6-8 that A_g , B_g and $C_g/\sqrt{Re_\tau}$ scale with Re_τ , and that the scaling of C_g is less obvious. In Figures 6 and 7 we also include the global log-law parameters found in [1], i.e. $A_{g,\log-\text{law}} = 1.52$ and $B_{g,\log-\text{law}} = 0.87$.

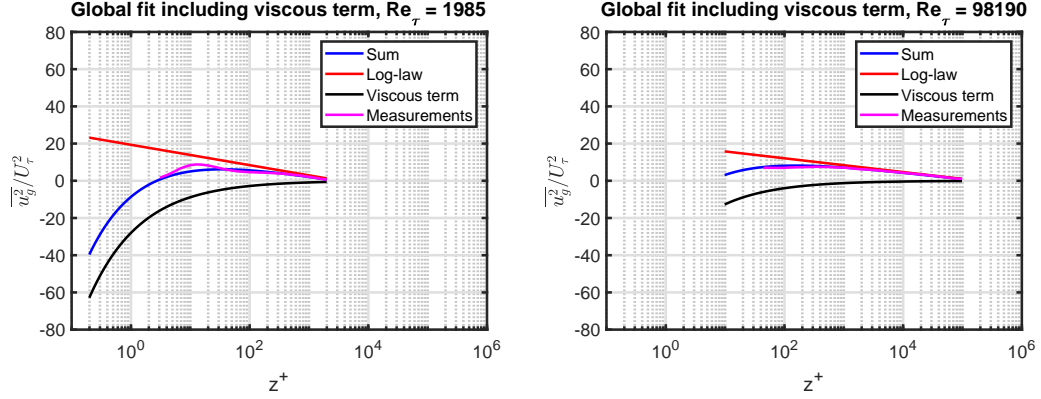


Figure 5: $\frac{\overline{u_g^2}(z)}{U_\tau^2}$ using Equation (1) and the global fit parameters as a function of z^+ . Left-hand plot: Lowest measured Re_τ , right-hand plot: Highest measured Re_τ .

It is not shown here, but we have attempted both log- and power-law fits to the parameters without finding a satisfactory match. Instead, the best fit is found using an expression including hyperbolic tangent:

$$Q(Re_\tau) = a + b \times \tanh(c \times [Re_\tau - d]), \quad (23)$$

where Q is the quantity to fit and (a, b, c, d) are fit parameters. Note that we have also tested using the tangent function, but hyperbolic tangent is marginally better. The resulting fit parameters are collected in Table 1; the values for d indicate the transitional Reynolds number which is around 11000-12000 for A_g and $C_g/\sqrt{Re_\tau}$ but lower for B_g . Perhaps this difference is because B_g depends on the specific geometry, i.e. a pipe for our case.

The fits are to the smooth wall pipe measurements, but the rough wall measurements are shown for reference.

Asymptotic values for the fit parameters are:

$$\lim_{Re_\tau \rightarrow \infty} A_g = 1.60 \quad (24)$$

$$\lim_{Re_\tau \rightarrow \infty} B_g = 0.96 \quad (25)$$

$$\lim_{Re_\tau \rightarrow \infty} C_g/\sqrt{Re_\tau} = 0.12, \quad (26)$$

where Equation (26) implies that:

$$\lim_{Re_\tau \rightarrow \infty} C_g = 0.12 \times \sqrt{Re_\tau} \quad (27)$$

For C_g (left-hand plot in Figure 8) it is interesting to note the non-monotonic variation with Re_τ ; this appears to be a transition between two different scalings for low and high Reynolds numbers, see Section 5.1. Possibly the inner peak dominates for lower Reynolds numbers and the outer peak for higher Reynolds numbers, see Section 5.1.

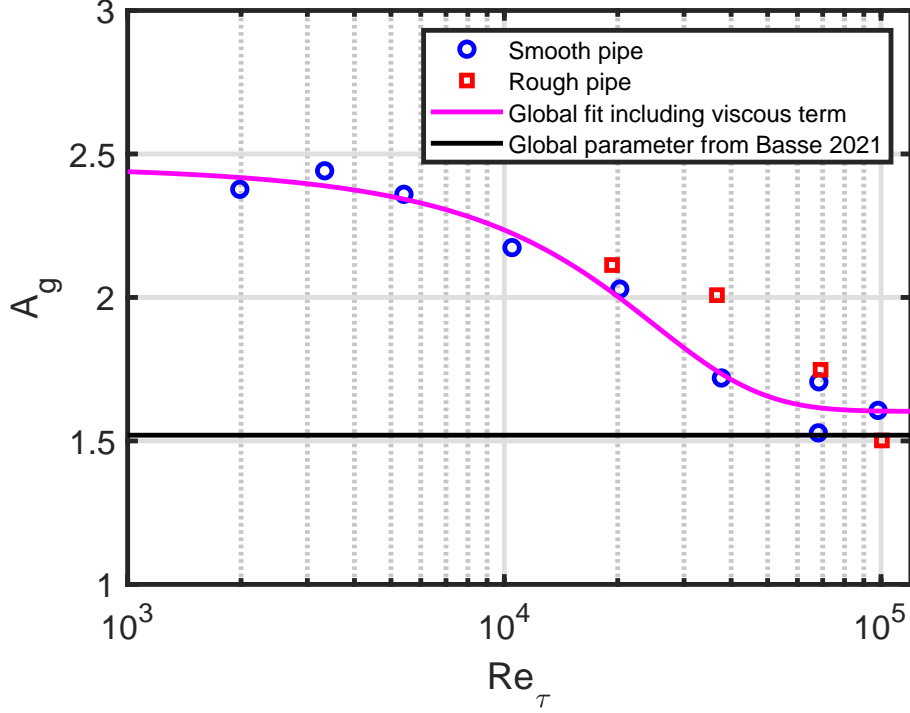


Figure 6: A_g as a function of Re_τ .

Table 1: Fits to parameters using Equation (23).

Parameter	a	b	c	d
A_g	2.21	-0.60	3.97e-5	11186
B_g	1.28	-0.32	5.85e-5	4609
$C_g/\sqrt{Re_\tau}$	1.03	-0.91	3.30e-5	-11755

4.4. Average fits

The decomposition of the fluctuations into a log-law and a viscous term is shown for the AA case in the left-hand plot of Figure 9. It is clear that the viscous term decreases with increasing Reynolds number, i.e. the viscosity contribution becomes less important.

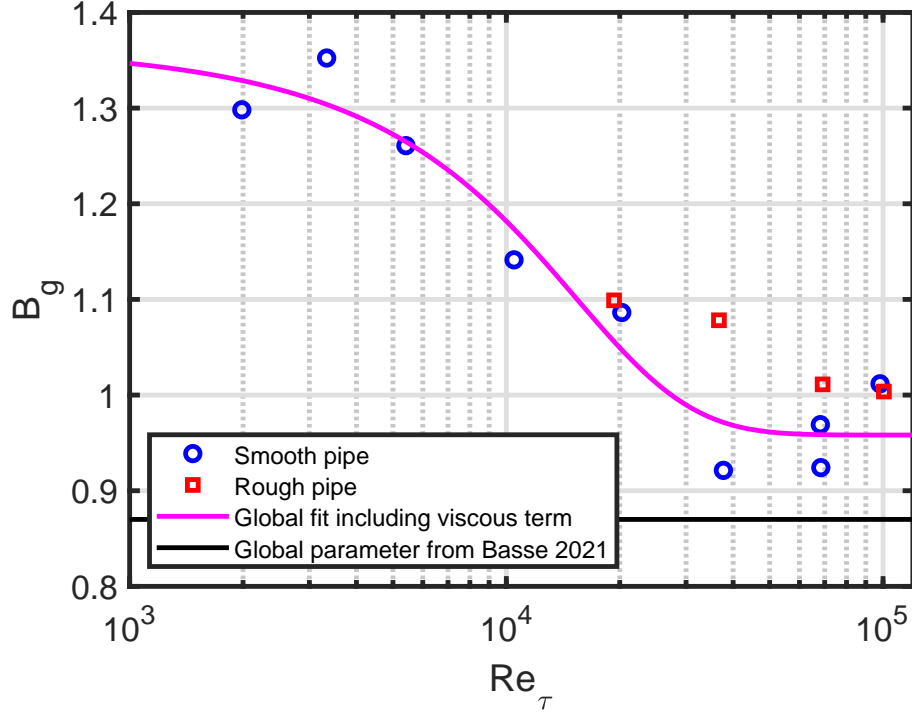


Figure 7: B_g as a function of Re_τ .

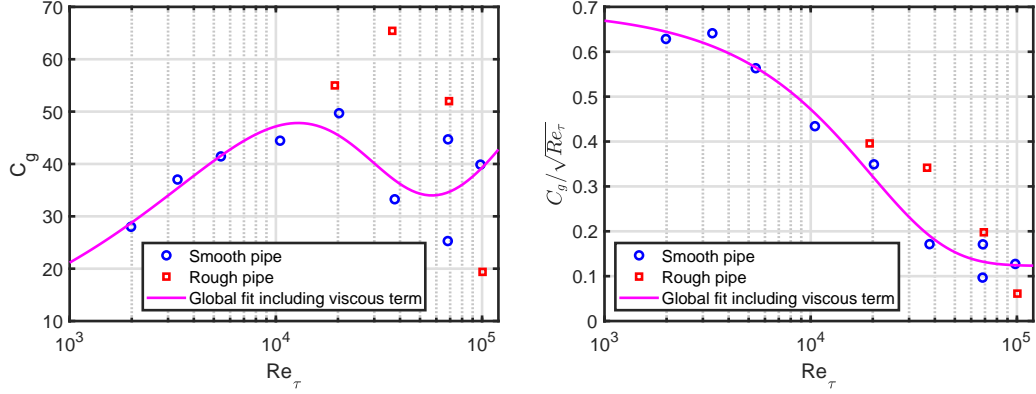


Figure 8: Left-hand plot: C_g as a function of Re_τ , right-hand plot: $C_g/\sqrt{Re_\tau}$ as a function of Re_τ .

Corresponding tanh fits, both using the individual parameter fits and a fit to the average, are included in the right-hand plot of Figure 9. The fits are made to the smooth pipe measurements, and we observe that this fit is not a perfect match for the rough pipe measurements.

Fits for the averages can be found in Table 2. The transitional Reynolds numbers are in the range 22000-26000 which is roughly a factor of two higher

than for the individual parameters. We also note that the individual parameter fits decrease for low Reynolds number which can not be captured by the average fits.

Figures illustrating similar results for the AM and VA cases can be found in Appendix A. We focus on AA here since it will be used for the turbulence intensity scaling in Section 5.4.

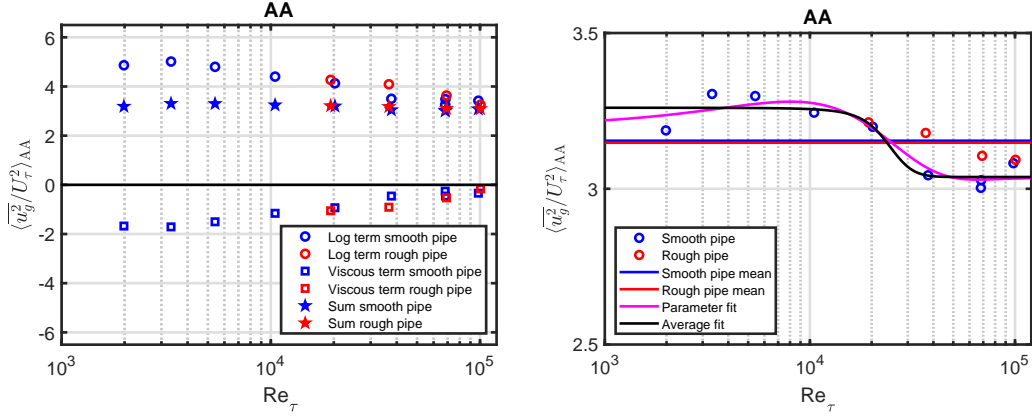


Figure 9: Left-hand plot: Decomposition of the AA average as a function of Re_τ . Right-hand plot: Fit to the sum using Equation (23), both for the parameters and the average.

Table 2: Fits to averages using Equation (23).

Average	a	b	c	d
$\langle \frac{u_g^2}{U_\tau^2} \rangle_{AM}$	2.39	-0.078	1.60e-4	22266
$\langle \frac{u_g^2}{U_\tau^2} \rangle_{AA}$	3.15	-0.11	1.40e-4	23677
$\langle \frac{u_g^2}{U_\tau^2} \rangle_{VA}$	3.62	-0.12	1.18e-4	26398

A comparison of the log-law and viscous terms for local and global fits is available in Figure 10. The magnitude of the viscous term is much larger for the global fit than for the local fit and has a non-zero asymptotic value. The global log-law term decreases with increasing Reynolds number and crosses the local log-law term at $Re_\tau \sim 20000$. We conclude that the main difference is due to the behaviour of the viscous term.

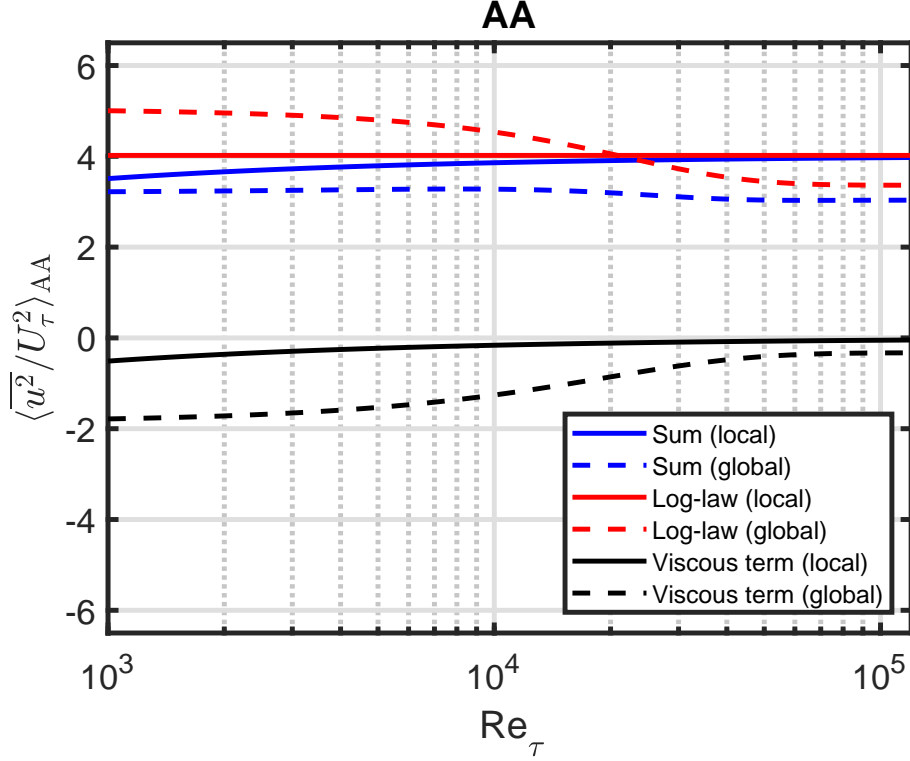


Figure 10: Decomposition of the AA average as a function of Re_τ . Local fit is solid lines, global fit is dashed lines.

5. Discussion

5.1. Peak scaling

Our introduction of the global peak as a mathematical abstraction is meant to capture turbulence production, both clearly identified as an inner peak and also - more controversially - as an outer peak which might emerge for high Reynolds numbers. It has e.g. been proposed that the outer peak is consequence of an invalid use of Taylor's "frozen turbulence" hypothesis [16]. Here, a single convection velocity is assumed for all eddy scales at a given point. However, "It is suspected that the larger-scale coherent attached eddies are convected downstream at a faster rate than the smaller-scale coherent eddies" [4].

We propose that the global peak captures both behaviour of the established inner peak and a corresponding outer peak if it exists: The inner (outer) peak dominates for lower (higher) Reynolds numbers, respectively. One issue is that for high Reynolds numbers, the inner peak is not captured which leads to a risk that the measurements become biased towards the pipe axis.

We will show results in Figures 11 and 12. The only difference between the figures is the maximum Reynolds number, which is 1.2×10^5 and 10^8 , respectively.

5.1.1. Peak position

The normalized distance from the wall z^+ for the various peak definitions is shown in the left-hand plots of Figures 11 and 12.

Two values which are independent of Re_τ , as defined in Equations (6) and (7), are included.

Two additional peak positions which scale with Re_τ are shown, one is the outer peak (or intersection) scaling from [13]:

$$z^+|_{\text{outer peak}} = 32.66 \times Re_\tau^{0.27}, \quad (28)$$

and the other is the global peak scaling, which has the asymptotic behaviour:

$$\lim_{Re_\tau \rightarrow \infty} z^+|_{\text{global peak}} = \left(\frac{\lim_{Re_\tau \rightarrow \infty} C_g}{2 \times \lim_{Re_\tau \rightarrow \infty} A_g} \right)^2 \quad (29)$$

$$= 1.41 \times 10^{-3} \times Re_\tau \quad (30)$$

5.1.2. Peak amplitude

If we first focus on the inner peak amplitude, earlier results propose either a log-law [13] scaling:

$$\left. \frac{\overline{u^2}}{U_\tau^2} \right|_{\text{inner peak, log-law}} = 0.646 \times \log(Re_\tau) + 3.54 \quad (31)$$

or a power-law scaling [17]:

$$\left. \frac{\overline{u^2}}{U_\tau^2} \right|_{\text{inner peak, power-law}} = 11.5 - 19.32 \times Re_\tau^{-1/4} \quad (32)$$

Both scalings are shown in the right-hand plots of Figures 11 and 12 and deviate visibly above $Re_\tau \sim 10000$ [1]. Global peak scalings from Equation (9) and our global fit:

$$\left. \frac{\overline{u_g^2}}{U_\tau^2} \right|_{\text{global peak}} = B_g - 2A_g \times (1 + \log(C_g) - \log(2A_g)) + A_g \log(Re_\tau) \quad (33)$$

are also included along with the outer peak (or intersection) scaling from [13]:

$$\left. \frac{\overline{u^2}}{U_\tau^2} \right|_{\text{outer peak, log-law}} = 0.99 \times \log(Re_\tau) - 3.06, \quad (34)$$

which is quite similar to Equation (9) for high Reynolds number where the constant becomes negligible.

It is interesting to note that the asymptotic value of our global fit is a constant:

$$\lim_{Re_\tau \rightarrow \infty} \left. \frac{\overline{u_g^2}}{U_\tau^2} \right|_{\text{global peak}} = 8.20 \quad (35)$$

Thus, the position of the global peak increases without bound, but the corresponding amplitude is bounded.

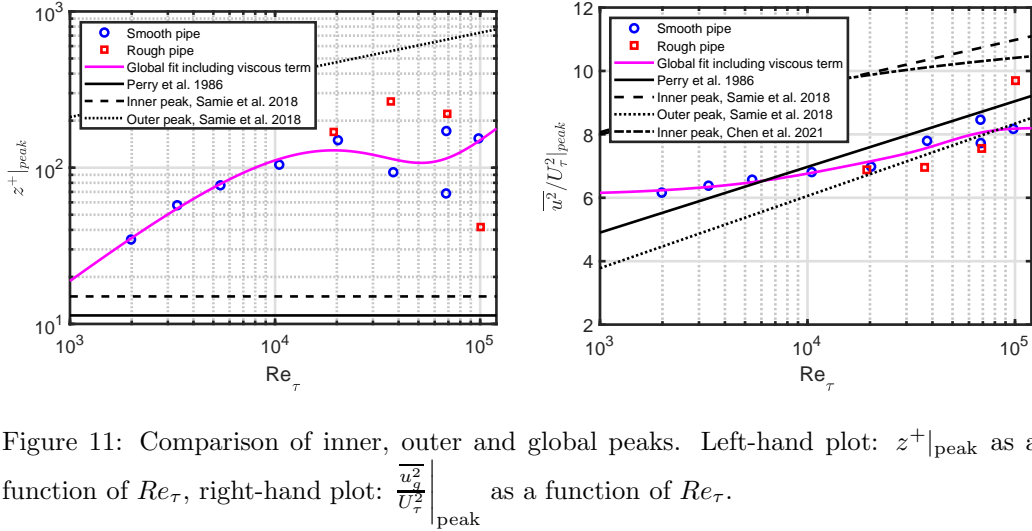


Figure 11: Comparison of inner, outer and global peaks. Left-hand plot: $z^+|_{\text{peak}}$ as a function of Re_τ , right-hand plot: $\left. \frac{\overline{u_g^2}}{U_\tau^2} \right|_{\text{peak}}$ as a function of Re_τ .

5.2. Asymptotic behaviour of the viscous term

Since the asymptotic value of $C_g/\sqrt{Re_\tau}$ is finite and non-zero, viscosity - or a similar effect - remains of importance. This finite value also leads to the fact that the global peak amplitude approaches a constant value. It is unclear whether this is a viscosity effect or another physical phenomenon, e.g. a vortex effect [18]: Here, it is found that "anomalous energy dissipation" is only found for pipe flow if the walls are rough. However, we do not see a

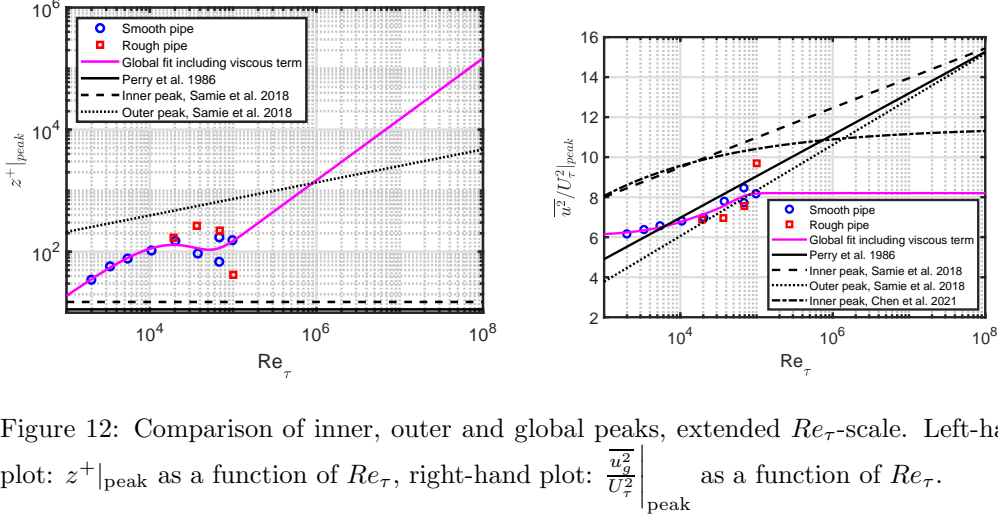


Figure 12: Comparison of inner, outer and global peaks, extended Re_τ -scale. Left-hand plot: $z^+|_{peak}$ as a function of Re_τ , right-hand plot: $\frac{u_g^2}{U_\tau^2}|_{peak}$ as a function of Re_τ .

clear distinction of the viscous term when we compare the smooth and rough pipe results.

Our research supports the finding that the viscous effect exists for both smooth and rough pipes. This is in line with the fact that we have previously shown that the TI scales with friction factor, which has a finite value for both smooth and rough pipes.

5.3. Davidson-Krogstad model

An alternative log-law model for streamwise velocity fluctuations which does not interpret the results as attached eddies has been proposed by Davidson and Krogstad (DK) [19]. The resulting equation for the streamwise fluctuations in the log-law region has a structure similar to Equation (1) with:

$$A_{l,DK} = 0.91 \quad (36)$$

$$B_{l,DK} = 1.36 - 0.91 \times \log(P/\varepsilon) \quad (37)$$

$$C_{l,DK} = 3.88 \times (P/\varepsilon)^{-1/2}, \quad (38)$$

where P is the rate of turbulent energy production and ε is the energy dissipation rate. Thus, we can estimate a global average of $\langle P/\varepsilon \rangle$ by comparing our global fit to the local DK model:

$$B_g = 1.36 - 0.91 \times \log\langle P/\varepsilon \rangle \quad (39)$$

$$\langle P/\varepsilon \rangle = \exp(1.49 - B_g/0.91) \quad (40)$$

The result of the comparison can be found in Figure 13. The local/global comparison appears to yield reasonable results, where $\langle P/\varepsilon \rangle$ is around one for low Reynolds numbers (production balances dissipation), but rises to a higher plateau for high Reynolds numbers (production is around 1.5 times dissipation).

Using $\langle P/\varepsilon \rangle$ based on B_g for the DK model implies that both $B_{l,\text{DK}}$ and $C_{l,\text{DK}}$ decrease with increasing Reynolds number; for the global parameters, we also see a decrease of B_g , but an increase for C_g . This points to the main differences between local and global behaviour being due to the viscous term.

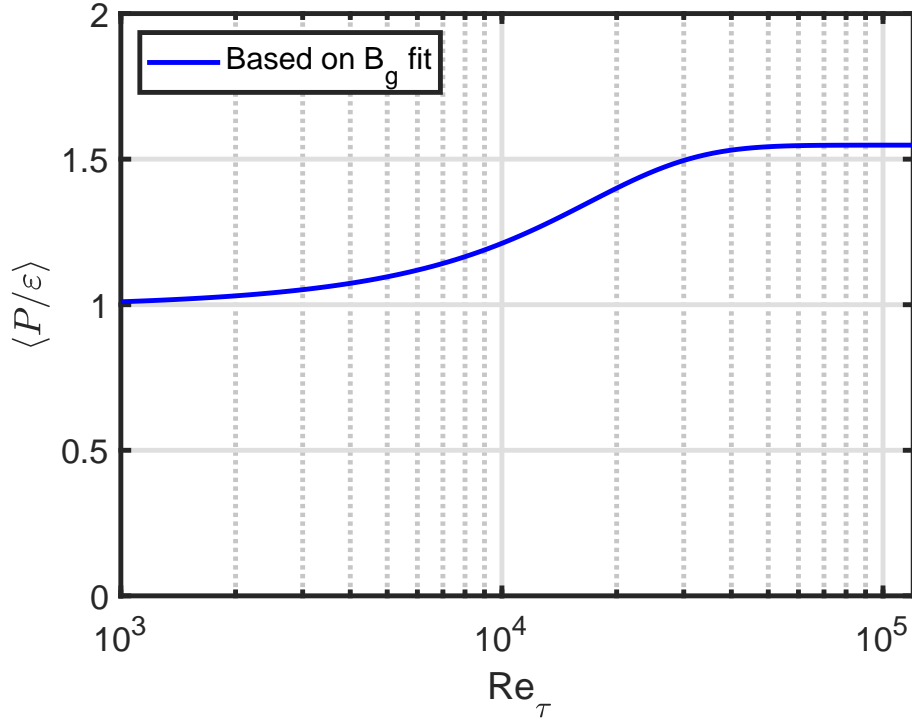


Figure 13: Predicted $\langle P/\varepsilon \rangle$ as a function of Re_τ .

5.4. Turbulence intensity scaling with friction factor

Our results have an impact on the friction factor scaling of TI, see Figure 14. Here, we have assumed that:

$$\frac{\langle I_g^2 \rangle_{\text{AA}}}{\lambda} = \frac{1}{8} \times \left\langle \frac{\overline{u_g^2}}{U_\tau^2} \right\rangle_{\text{AA}} \quad (41)$$

However, our result is above the measurements, since the assumption that:

$$\lambda = 8 \times \left\langle \frac{U_\tau^2}{U_g^2} \right\rangle_{\text{AA}} \quad (42)$$

is not accurate, see Figure 15.

The rough pipe results deviate from smooth pipe results since we derive from AA results, see the right-hand plot in Figure 9.

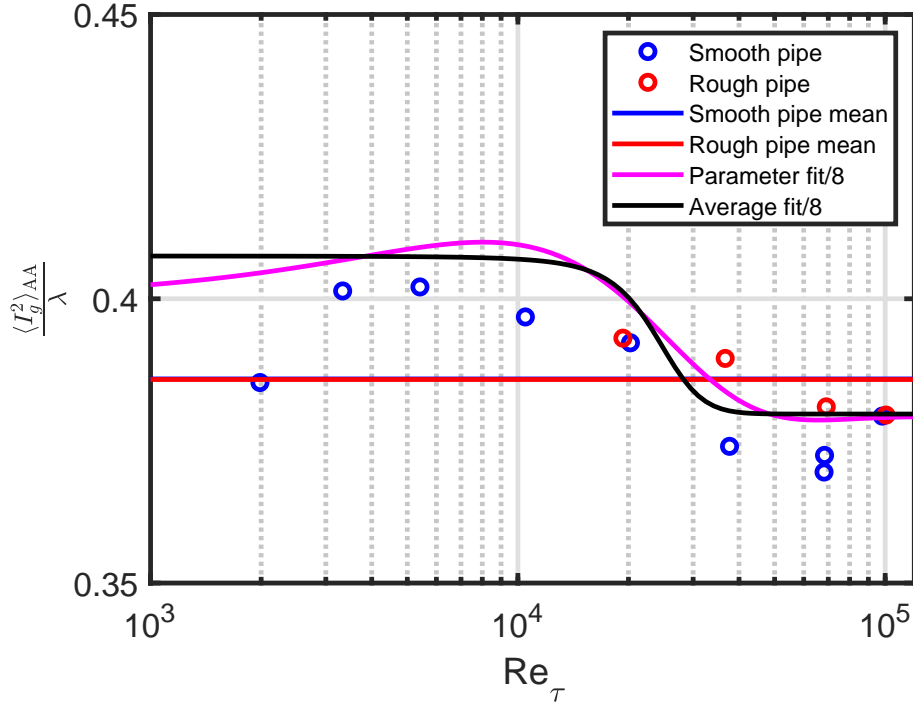


Figure 14: $\frac{\langle I_g^2 \rangle_{\text{AA}}}{\lambda}$ as a function of Re_τ . Mean values of the measurements are shown along with parameter and average fits - divided by 8 - from the right-hand plot of Figure 9.

6. Conclusions

We have introduced a global model of the streamwise velocity fluctuations in pipe flow calibrated to Princeton Superpipe measurements. The model includes both a log-law and a viscous term. The global model captures the overall behaviour of the fluctuations but is a physical abstraction with the main purpose of quantifying turbulence intensity scaling with Reynolds

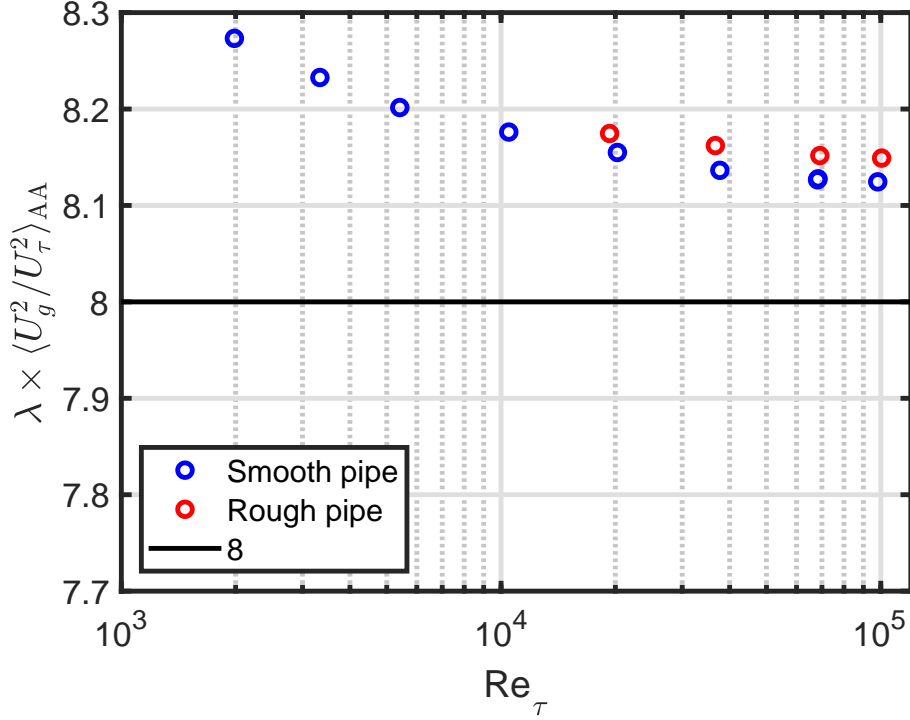


Figure 15: Variation of $\lambda \times \left\langle \frac{U_g^2}{U_\tau^2} \right\rangle_{AA}$ as a function of Re_τ .

number. The model has a single global peak, which is bounded and captures both the inner and outer peaks. In reality, the flow transitions from a lower Reynolds number inner peak dominated flow to a higher Reynolds number outer peak dominated flow.

The parameters can be represented by hyperbolic tangent fits, and exhibit a transition region for $Re_\tau \sim 11000 - 12000$ (parameter fits) or $Re_\tau \sim 22000 - 26000$ (average fits). This is consistent with a simultaneous modification of fluctuation and mean velocities, i.e including a viscous term clarifies that there is indeed a Reynolds number transition for fluctuations as we have previously shown for the mean flow [1].

The impact of our findings include peak scaling, the finite non-zero asymptotic value of the viscous term, turbulent energy production/dissipation and turbulence intensity scaling. Finally, we show in Appendix B that including a wake term does not lead to a clear transition; rather, the model reverts to being similar to a two-parameter power-law.

Acknowledgements. We thank Professor Alexander J. Smits for making the Princeton Superpipe data publicly available.

Data availability statement. Data sharing is not applicable to this article as no new data were created or analyzed in this study.

Appendix A. Local and global average fits

For reference, average fits for the AM and VA are collected here. The decomposition of the fluctuations into a log-law and a viscous term is shown for the AM and VA cases in the left-hand plots of Figures A.16-A.17. Corresponding tanh fits, both using the individual parameter fits and a fit to the average, are included in the right-hand plots of Figures A.16-A.17.

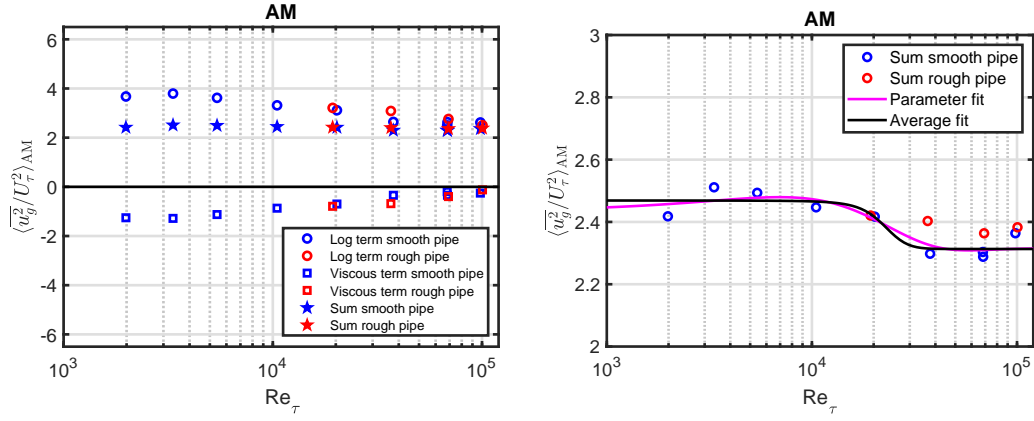


Figure A.16: Left-hand plot: Decomposition of the AM average as a function of Re_τ . Right-hand plot: Fit to the sum using Equation (23), both for the parameters and the average.

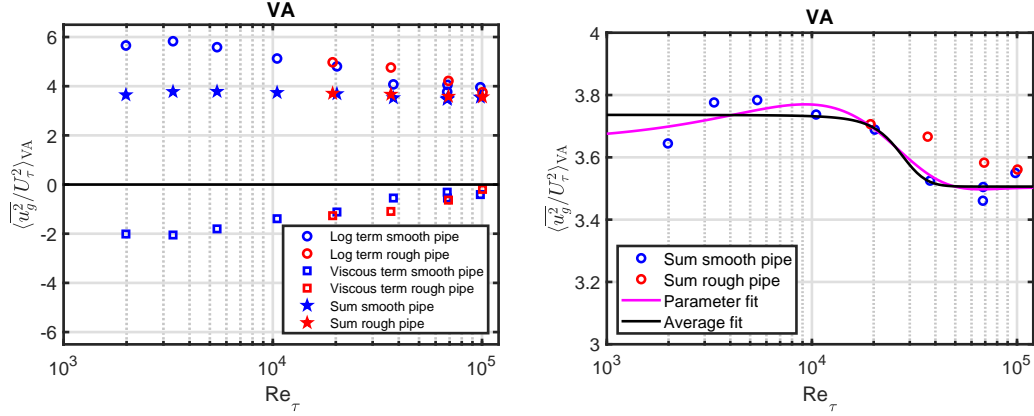


Figure A.17: Left-hand plot: Decomposition of the VA average as a function of Re_τ . Right-hand plot: Fit to the sum using Equation (23), both for the parameters and the average.

A comparison of the log-law and viscous terms for local and global fits is available in Figures A.18-A.19 for the AM and VA cases.

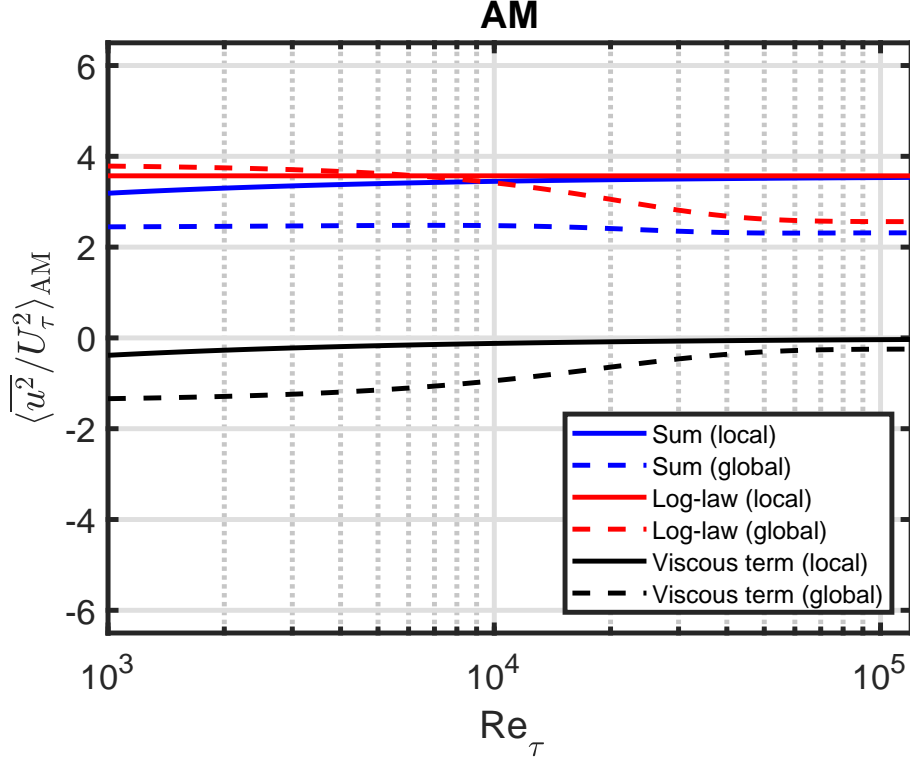


Figure A.18: Decomposition of the AM average as a function of Re_τ . Local fit is solid lines, global fit is dashed lines.

Appendix B. Inclusion of the wake term

As mentioned in Section 2, we have also carried out our analysis for the case where a wake term is included in addition to the viscous term [10, 11, 12].

Appendix B.1. Model

Equation (1) is modified to:

$$\frac{\overline{u_l^2}(z)}{U_\tau^2} = B_l - A_l \log(z/\delta) + V(z^+) - W(z/\delta), \quad (\text{B.1})$$

where

$$W(z/\delta) = B_l(z/\delta)^2(3 - 2z/\delta) - A_l(z/\delta)^2(1 - z/\delta)(1 - 2z/\delta) \quad (\text{B.2})$$

is the wake term. Analytical integration of Equation (B.2) using Equations (10)-(15) yields these three equations:

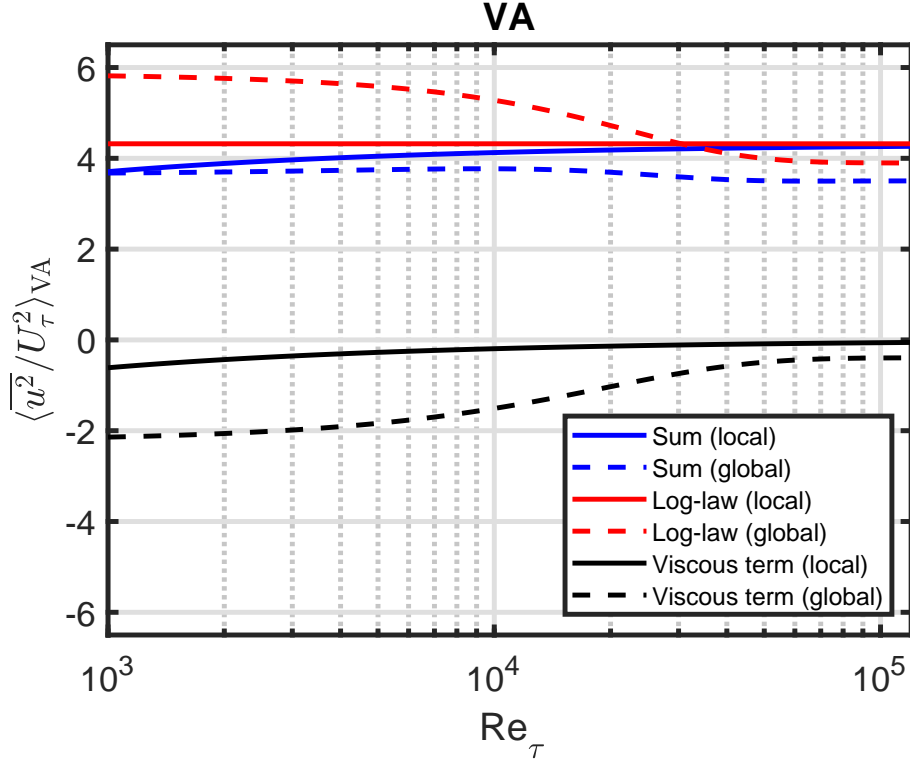


Figure A.19: Decomposition of the VA average as a function of Re_τ . Local fit is solid lines, global fit is dashed lines.

$$\langle W_g \rangle_{AM} = \frac{1}{2} \times B_{g,wake} + \frac{1}{60} \times A_{g,wake} \quad (B.3)$$

$$\langle W_g \rangle_{AA} = \frac{3}{10} \times B_{g,wake} \quad (B.4)$$

$$\langle W_g \rangle_{VA} = \frac{1}{5} \times B_{g,wake} - \frac{1}{140} A_{g,wake} \quad (B.5)$$

Combining these results with the analytical integration only including the viscous term leads to:

$$\left\langle \frac{\overline{u_g^2}}{U_\tau^2} \right\rangle_{AM,wake} = \frac{1}{2} \times B_{g,wake} + \frac{59}{60} \times A_{g,wake} - \frac{2C_{g,wake}}{\sqrt{Re_\tau}} \quad (B.6)$$

$$\left\langle \frac{\overline{u_g^2}}{U_\tau^2} \right\rangle_{AA,wake} = \frac{7}{10} \times B_{g,wake} + \frac{3}{2} \times A_{g,wake} - \frac{8C_{g,wake}}{3\sqrt{Re_\tau}} \quad (B.7)$$

$$\left\langle \frac{\overline{u_g^2}}{U_\tau^2} \right\rangle_{\text{VA,wake}} = \frac{4}{5} \times B_{g,\text{wake}} + \frac{767}{420} \times A_{g,\text{wake}} - \frac{16C_{g,\text{wake}}}{5\sqrt{Re_\tau}} \quad (\text{B.8})$$

The solutions to these three equations are:

$$A_{g,\text{wake}} = -\frac{1120}{177} \times \left\langle \frac{\overline{u_g^2}}{U_\tau^2} \right\rangle_{\text{AM,wake}} + \frac{700}{177} \times \left\langle \frac{\overline{u_g^2}}{U_\tau^2} \right\rangle_{\text{VA,wake}} \quad (\text{B.9})$$

$$B_{g,\text{wake}} = -\frac{2200}{531} \times \left\langle \frac{\overline{u_g^2}}{U_\tau^2} \right\rangle_{\text{AM,wake}} + 30 \times \left\langle \frac{\overline{u_g^2}}{U_\tau^2} \right\rangle_{\text{AA,wake}} \quad (\text{B.10})$$

$$-\frac{11900}{531} \times \left\langle \frac{\overline{u_g^2}}{U_\tau^2} \right\rangle_{\text{VA,wake}} \quad (\text{B.11})$$

$$C_{g,\text{wake}} = \sqrt{Re_\tau} \quad (\text{B.12})$$

$$\times \left(-\frac{1645}{354} \times \left\langle \frac{\overline{u_g^2}}{U_\tau^2} \right\rangle_{\text{AM,wake}} + \frac{15}{2} \times \left\langle \frac{\overline{u_g^2}}{U_\tau^2} \right\rangle_{\text{AA,wake}} - \frac{1295}{354} \times \left\langle \frac{\overline{u_g^2}}{U_\tau^2} \right\rangle_{\text{VA,wake}} \right) \quad (\text{B.13})$$

Appendix B.2. Parameter fits

The fits to the wake parameters are shown in Figures B.20-B.22. $A_{g,\text{wake}}$ is negative, which means that the slope of the log-law changes sign. For both $A_{g,\text{wake}}$ and $B_{g,\text{wake}}$, no strong variation with Re_τ is observed. In contrast, $C_{g,\text{wake}}$ has a strong scaling with Re_τ . In addition it is negative, so the viscous term becomes positive which is unphysical. The result is an equation with the functional form very similar to Equation (4).

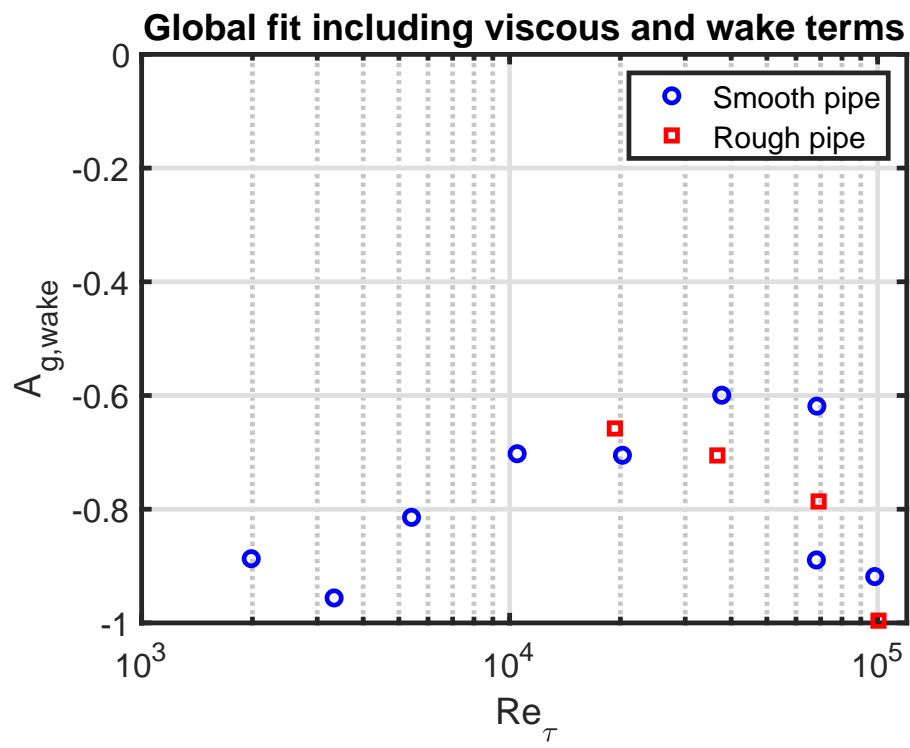


Figure B.20: $A_{g,wake}$ as a function of Re_τ .

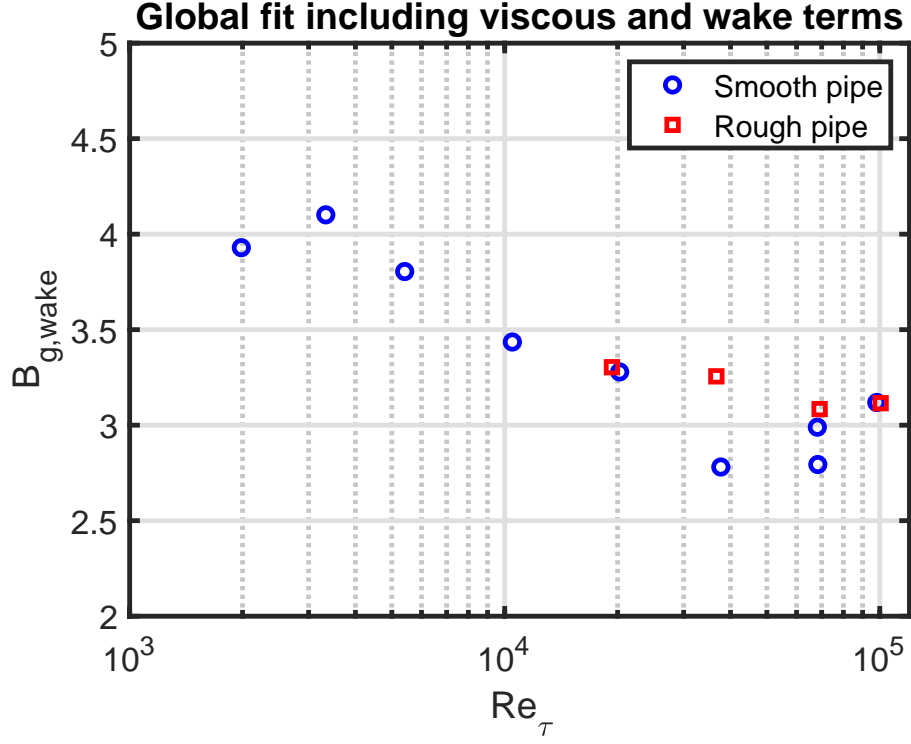


Figure B.21: $B_{g,wake}$ as a function of Re_τ .

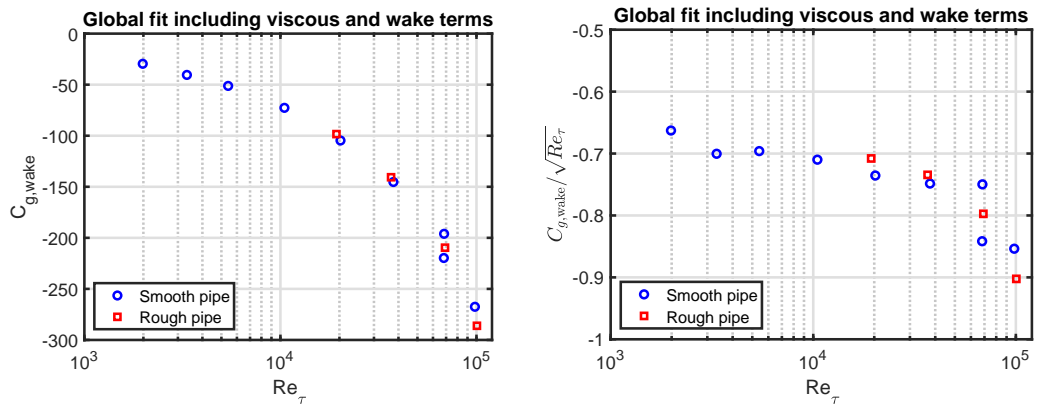


Figure B.22: Left-hand plot: $C_{g,wake}$ as a function of Re_τ , right-hand plot: $C_{g,wake}/\sqrt{Re_\tau}$ as a function of Re_τ .

References

- [1] Basse NT. Scaling of global properties of fluctuating and mean stream-wise velocities in pipe flow: Characterization of a high Reynolds number transition region. *Phys. Fluids* **33**, 065127 (2021).
- [2] Hultmark M, Vallikivi M, Bailey SCC and Smits AJ. Logarithmic scaling of turbulence in smooth- and rough-wall pipe flow. *J. Fluid Mech.* **728**, 376-395 (2013).
- [3] Perry AE and Chong MS. On the mechanism of wall turbulence. *J. Fluid Mech.* **119**, 173-217 (1982).
- [4] Perry AE, Henbest S and Chong MS. A theoretical and experimental study of wall turbulence. *J. Fluid Mech.* **165**, 163-199 (1986).
- [5] Townsend AA. The structure of turbulent shear flow, 2nd Ed. Cambridge University Press (1976).
- [6] Smits AJ, McKeon BJ and Marusic I. High-Reynolds number wall turbulence. *Annu. Rev. Fluid Mech.* **43**, 353-375 (2011).
- [7] Marusic I and Monty JP. Attached eddy model of wall turbulence. *Annu. Rev. Fluid Mech.* **51**, 49-74 (2019).
- [8] Perry AE, Hafez S and Chong MS. A possible reinterpretation of the Princeton superpipe data. *J. Fluid Mech.* **439**, 395-401 (2001).
- [9] Spalart PR. Direct simulation of a turbulent boundary layer up to $R_\theta = 1410$. *J. Fluid Mech.* **187**, 61-98 (1988).
- [10] Marusic I, Uddin AKM and Perry AE. Similarity law for the streamwise turbulence intensity in zero-pressure-gradient turbulent boundary layers. *Phys. Fluids* **9**, 3718-3726 (1997).
- [11] Marusic I and Kunkel GJ. Streamwise turbulence intensity formulation for flat-plate boundary layers. *Phys. Fluids* **15**, 2461-2464 (2003).
- [12] Kunkel GJ and Marusic I. Study of the near-wall-turbulent region of the high-Reynolds-number boundary layer using an atmospheric flow. *J. Fluid Mech.* **548**, 375-402 (2006).
- [13] Samie M, Marusic I, Hutchins N, Fu MK, Fan Y, Hultmark M and Smits AJ. Fully resolved measurements of turbulent boundary layer flows up to $Re_\tau = 20000$. *J. Fluid Mech.* **851**, 391-415 (2018).

- [14] Pirozzoli S, Romero J, Fatica M, Verzicco R and Orlandi P. One-point statistics for turbulent pipe flow up to $Re_\tau \approx 6000$. J. Fluid Mech. **926**, A28 (2021).
- [15] Smits AJ, Hultmark M, Lee M, Pirozzoli S and Wu X. Reynolds stress scaling in the near-wall region of wall-bounded flows. J. Fluid Mech. **926**, A31 (2021).
- [16] Taylor GI. The spectrum of turbulence. Proc. R. Soc. Lond. A **164**, 476-490 (1938).
- [17] Chen X and Sreenivasan KR. Reynolds number scaling of the peak turbulence intensity in wall flows. J. Fluid Mech. **908**, R3 (2021).
- [18] Eyink GL. Josephson-Anderson relation and the classical D'Alembert paradox. Phys. Rev. X **11**, 031054 (2021).
- [19] Davidson PA and Krogstad P-Å. A simple model for the streamwise fluctuations in the log-law region of a boundary layer. Phys. Fluids **21**, 055105 (2009).